

Influence of mosaic patterns in filament-wound tubes on mechanical behaviour under axial compression loading^{*})

Paweł Stabla^{1),**)} (ORCID ID: 0000-0001-6891-582X), Michał Smolnicki¹⁾ (0000-0003-1489-1062), Szymon Duda¹⁾ (0000-0002-5046-5485), Paweł Zielonka¹⁾ (0000-0002-1178-3368), Karolina Paczkowska¹⁾ (0009-0007-4170-3406), Zuzanna Pacholec¹⁾, Michał Barcikowski¹⁾ (0000-0001-5135-7892), Wojciech Błażejowski¹⁾ (0000-0001-9260-1388)

DOI: <https://doi.org/10.14314/polimery.2024.11.8>

Abstract: This study employs axial compression testing to analyze the impact of mosaic patterns on the mechanical properties, specifically the strength and stiffness, of composite tubes. Three mosaic patterns (1/1, 2/1, and 3/1) and three winding angles (45°, 55°, and 75°) were selected for evaluation. Additionally, the acoustic emission (AE) technique was utilized to investigate the damage mechanisms occurring in the composite structures. The results showed that the higher the mosaic pattern the higher the stiffness and strength of the composite tubes under axial compression loading.

Keywords: filament winding, axial compression, mosaic pattern, acoustic emission.

Wpływ wzoru mozaikowego w rurach nawijanych włóknami na właściwości mechaniczne w warunkach obciążenia ściskającego osiowego

Streszczenie: W niniejszej pracy zastosowano testy osiowego ściskania w celu analizy wpływu wzorów mozaikowych na właściwości mechaniczne, w szczególności wytrzymałość i sztywność, rur kompozytowych. Wybrano do oceny trzy wzory mozaikowe (1/1, 2/1 oraz 3/1) oraz trzy kąty nawijania (45°, 55° i 75°). Dodatkowo, użyto technikę emisji akustycznej (AE) do badania mechanizmów uszkodzeń struktur kompozytowych. Wyniki pokazały, że im wyższy wzór mozaikowy, tym większa sztywność i wytrzymałość rur kompozytowych pod obciążeniem osiowego ściskania.

Słowa kluczowe: nawijanie włókien, ściskanie osiowe, wzór mozaikowy, emisja akustyczna.

Filament winding (FW) technique is a method, in which fiber band, impregnated with resin, is wound continuously on a rotating mandrel. The mandrel rotates along its axis, and the feed eye (also known as pay-out eye), which delivers the fiber band, moves back and forward along the mandrel's axis. This is the basic method with just 2 degrees of freedom. In more advanced winders, additional degrees of freedom are added. Namely, the rotation of the feed eyelet and the possibility of moving it closer or further away from the mandrel. The last additional movement is especially useful in composite pressure vessel winding [1, 2].

In filament winding, the pay-out eye moves forward and backwards along the mandrel axis. This process is executed periodically, up to the moment when the mandrel is fully covered by the impregnated fiber. Due to that fact, the subsequent bands are deposited in a way shown in Figure 1, where a circuit is divided into forward and backward strokes. The second circuit is placed next to the first one, or in a different circumferential localization, depending on the mosaic pattern.

Most of the research attempts have been conducted using layered or sub-layered modelling approaches. The methods described concentrate only on the winding angle as an important technological parameter in the filament winding technique. In the first case, the complex helical layer with winding angle is simplified to one layer with just a positive or negative winding angle and the same thickness.

The discussed method has been widely incorporated into various research. It is one of the main methods for analyzing composite pressure vessels employing finite element method [3–7]. The presented approach is easy to

¹⁾ Wrocław University of Science and Technology, Faculty of Mechanical Engineering, Wybrzeże Wyspiańskiego 27, 50-370 Wrocław, Poland.

^{*}) Material contained in this article was presented at the XXI Scientific-Technical Conference on „Polimery i Kompozyty Konstrukcyjne” (KOMPOZYTY 2024), 22–25 October 2024, Wiśła, Poland.

^{**)} Author for correspondence: pawel.stabla@pwr.edu.pl

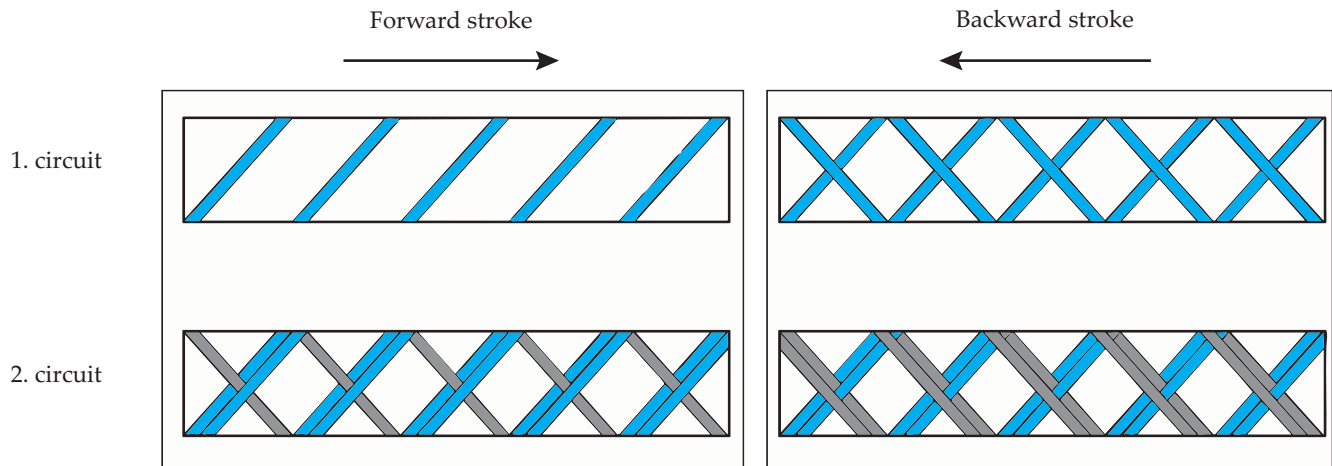


Fig. 1. Two circuits of filament winding process divided into forward and backward strokes

apply and does not require an additional effort connected with the geometry partitioning. The layout might even be uploaded from the external file.

Almeida Jr *et al.* [8] used the genetic algorithm to obtain the optimal stacking layout of a composite tube with the following dimensions: 381 mm length and 136 mm diameter. The researchers conducted numerical calculations with the finite element method using Abaqus 6.14 commercial software platform. The analysis considered non-linear geometry since large displacements and strains were predicated during the simulation. Martins *et al.* [9] conducted a comparative study between two loading conditions in terms of the hydrostatic test of internal pressure (closed-end and restrained-end condition). The research concentrated on the experimental part; however, it was concluded that the numerical results predicted satisfactorily the pressure failure distinguishing the matrix and fiber damage modes.

Azevedo *et al.* [10] described the process of mosaic pattern modelling, divided into cylinder modelling, datum plane creation, projection onto the cylinder surface and finally the complete partitioned cylinder creation. The numerical research was compared with the experimental tests of filament-wound composite tubes under axial compression loading.

Tales *et al.* [11] presented the numerical analysis using FEM updating to fit the damage evolution parameters. In the analysis, the authors used the mosaic approach to model FW tubes. Three mosaic patterns were considered: 1/1, 2/1 and 3/1. The numerical investigations of filament wound structures considering mosaic patterns were also conducted on pressure vessels. Akhtar *et al.* [12] compared the results of FEM simulations of three different patterns with the simple layered method. The stress distribution is highly influenced by the mosaic pattern number as well as the maximum values of stress along the fiber direction.

A more precise interpretation of filament-wound composite structure includes the zig-zag with interlacing line. The straight line is substituted by a polygonal chain. The proper definition of material layout in the zig-zag area

needs additional procedures which should somehow reflect the winding process in the finite element analysis. Thus, a special, additional script should be prepared and evaluated to obtain genuine material distribution. Otherwise, the model partitioning would be extremely time-consuming. Due to that fact, this approach is rarely found in literature.

Pourahmadi *et al.* [13, 14] investigated the effect of bandwidth using the mosaic approach with a zig-zag interlacing approach. They also developed their model for the undulation of fiber phenomena, but only at the repetitive unit cell (RUC) level. Their research was purely numerical, and the results were compared to calculations provided with the use of classical lamination theory, however, a significant difference has been observed in the mechanical response of composite tubes under internal pressure loading.

Ye *et al.* [15] described the parametric mesoscopic and multi-scale models of filament-wound structures to predict the mechanical response under axial tensile loading. As a result of their work, a numerical method for finite element analysis was proposed to facilitate the analysis of filament-wound composites. The analysis was performed on thick-wall specimens.

In this study, the influence of mosaic patterns on strength and stiffness of composite tubes is investigated. As is commonly disregarded, the results of the research may usefully contribute to the current state-of-the-art and give valuable suggestions regarding the design process for engineers and scientists.

EXPERIMENTAL PART

Materials

The material used in the presented work consists of Torayca T720SC carbon fiber (Toray, Tokyo, Japan) and Araldite LY1564 epoxy resin (Huntsman, USA) with Aradur 3474 hardener (Huntsman, USA). The basic parameters provided by producers are presented in Table 1.

Table 1. Material characteristics [16, 17]

Parameter	Value
Fiber	
Name	Torayca T720SC
Type	Carbon fiber
Filament	36k
Tensile strength, MPa	5880
Tensile modulus, GPa	265
Density, g/cm ³	1.8
Matrix	
Resin name	Araldite LY 1564
Hardener name	Aradur 3474
Resin type	thermoset
Formulation	100:26
Pot life at 40°C, min	60–70
Tensile strength, MPa	80
Tensile modulus, GPa	2900
Density, g/cm ³	1.1

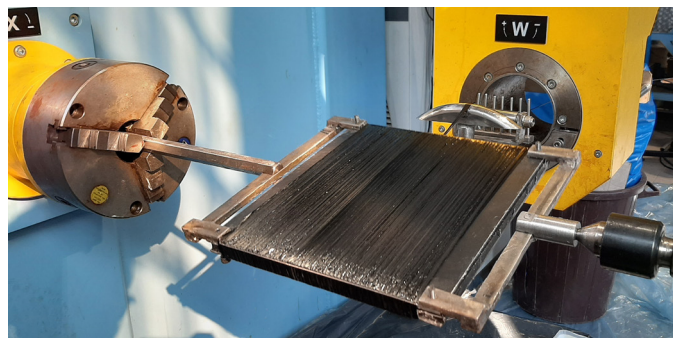
Sample preparation for testing

In material characterization, flat samples are used in various mechanical tests. Since filament winding is based on a roving material, it was decided to prepare filament-wound plates. The process is similar to the typical FW, with the difference that the mandrel is not an axisymmetric tube but a flat plate. In this work, a plate with dimensions of 25 × 25 cm was used. The manufacturing process is shown in Figure 2.

In the process, the hoop winding mode was chosen in the Winding Expert software. In this way, a unidirectional laminate can be wound with a winding angle close to 90°. After winding, the laminate with the plate mandrel was placed under a one-ton press until the resin consolidated (around 24 h). Next, the system was cured in the oven for 1 h at 80° and 4 h at 120°. The final step was cutting the laminate into specimens for each standard test.

Methods

Tensile tests were conducted according to ASTM D3039. Compression tests were performed for longitudinal and

**Fig. 2. Unidirectional flat laminate winding process**

transverse directions, following the standard ASTM D6641. The shear test was performed following ASTM D7078 standard using the V-notched rail shear method. brak nazwy urządzenia An axial compression test was conducted on MTS 809 (MTS Systems, Eden Prairie, MN, USA). The preliminary experiments show the problem with the insufficient stiffness of the edges which led to premature failure of the tested tube. To enhance the distribution of load and to stiffen the edges, an additional hand-laminated CFRP reinforcement was wound. After the consolidation of the overwrap, the edges were ground to remove any excessive laminates and to provide parallelism of the edges' surfaces. The final specimen is present in Figure 3.

**Fig. 3. FW pipe with additional reinforcement prepared for axial compression test**

In the research, nine configurations were analyzed. Three winding angles (45°, 55°, 75°) and three mosaic patterns (1/1, 2/1, 3/1) were chosen as it was described previously. The angle 45° is very commonly used in industry as it is believed to be the “mean” angle, merging hoop and polar winding. The angle 55° is typically used for pressure applications and is widely investigated so it enables comparison with another study. The angle 75° is the closest possible angle to the hoop winding in terms of the influence of the different mosaic patterns. Regarding the mosaic patterns, the limited number of bands to cover the whole circumference of the mandrel restricted the possible patterns. The geometric dimensions of each configuration are outlined in Table 2. The length and mass were measured, and the thickness was calculated using the known density.

To provide suitable mounting conditions, the experimental setup consisted of two platens, one with a spherical joint and another rigid. The specimen was mounted between the platens and initially loaded slightly to a value of around 50N. It is a common procedure in such tests to remove slacks from all force-displacement curves [18].

In the axial compression test, an acoustic emission technique was involved. Acoustic emission (AE) analysis was conducted using Vallen AMYS-6 (Vallen Systeme, Wolfratshausen, Germany). Two piezoelectric sensors capable of gathering signals between 100 and

T a b l e 2. Mass and geometric characteristics of samples subjected to axial compression test

Configuration	Mass g	Length mm	Thickness mm
45_1/1	14.55±0.98	150.07±0.14	0.5±0.03
45_2/1	16.41±0.26	150.04±0.12	0.56±0.01
45_3/1	18.91±0.11	149.81±0.10	0.65±0.01
55_1/1	14.46±0.32	149.78±0.11	0.5±0.01
55_2/1	14.55±0.44	149.50±0.19	0.5±0.02
55_3/1	14.69±0.39	149.98±0.26	0.51±0.01
75_1/1	15.31±0.40	149.58±0.16	0.53±0.01
75_2/1	13.83±0.11	149.96±0.17	0.48±0.01
75_3/1	14.32±0.30	149.69±0.21	0.49±0.01

T a b l e 3. Geometric parameters used in FEM analysis in axial compression test

Configuration	Length mm	Thickness mm
45_1/1	150.1	0.50
45_2/1	150.0	0.56
45_3/1	149.8	0.65
55_1/1	149.8	0.50
55_2/1	149.5	0.50
55_3/1	150.0	0.51
75_1/1	149.6	0.53
75_2/1	150.0	0.48
75_3/1	149.7	0.49

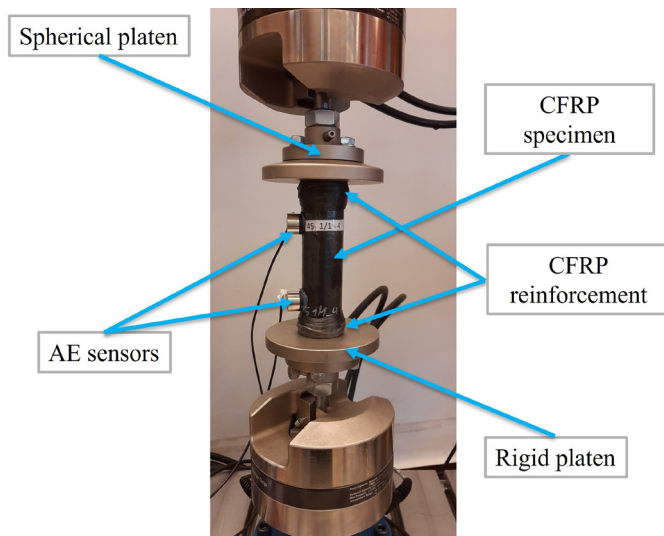


Fig. 4. Axial compression test device with mounted sample

450 kHz, were mounted on the specimen employing hot glue. The two wide-band preamplifiers were used (AEP5). Initially, apart from the AE signals analysis, the localizations of the events were under the interests of the research. Therefore, two sensors were attached to the specimen at a known distance. Unfortunately, due to the size of the sensors, the geometry of the specimen and the material anisotropy, the results of the localization algorithm were unreliable and are not present in the work. The experimental setup with the specimen and AE sensors is presented in Figure 4. The experiment was displacement-driven with a constant speed of 1 mm/min.

The numerical calculations were conducted in Abaqus software. Each configuration of winding angle and mosaic pattern was considered, so nine different models have been created. As it was described in previous sections, the material distribution was set using the Python script. The dimensions of each configuration were based on the measurements of physical specimens and are presented in Table 3.

Axial compression loading in FEA was designed to reflect the experiment and to bear in the simulation of time and effort. One of the most important issues in the axial

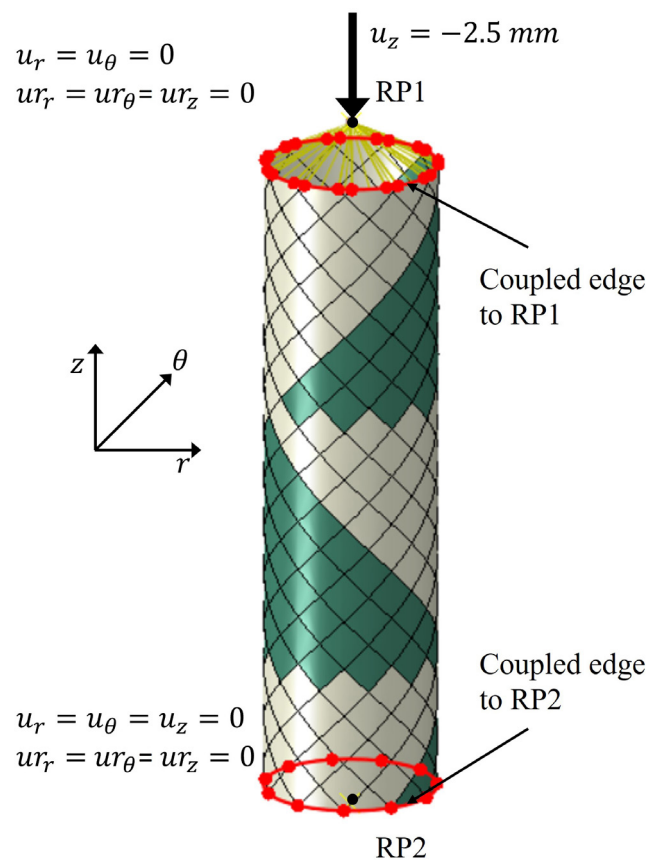


Fig. 5. FE model, definition of loads and boundary conditions in axial compression test

compression test was the loading and boundary conditions reflection. To avoid computational problems with contact definition, both plates are reflected by a reference point (RP) coupled to the edge of the tube. Next, RP responsible for the static plate is constrained, so that no displacements and rotations are possible. The RP from the moving is similarly restricted, except for the displacement in the axial direction. The experiment was displacement driven and the numerical analysis likewise. Figure 5 shows the boundary conditions and loads in axial compression.

As a complementary method to assess the damage mode occurring in the composite material, macroscopic and microscopic observations were conducted. The scan-

Table 4. Properties of filament-wound flat laminate

Property	Average	SD	CV
Longitudinal modulus of elasticity (E_1), GPa	148.00	6.63	0.04
Transverse modulus of elasticity (E_2), GPa	7.37	0.08	0.01
Shear modulus of elasticity (G_{12}), GPa	3.15	0.16	0.05
Poisson ratio (ν)	0.35	0.04	0.11
Tensile longitudinal strength (X_t), MPa	1762.7	73.1	0.04
Compression longitudinal strength (X_c), MPa	669.4	96.3	0.14
Tensile transverse strength (Y_t), MPa	31.5	2.2	0.07
Compression transverse strength (Y_c), MPa	123.2	5.4	0.04
Shear strength (S_{12}), MPa	57.2	0.8	0.02

ning electron microscope JEOL JSM-6610A with an acceleration voltage of 20 kV was used.

RESULTS AND DISCUSSION

Table 4 summarizes the mechanical tests performed to obtain the elastic and strength properties of filament-wound laminate. The results are presented as average values and corresponding standard deviations (SD) and coefficient of variation (CV) and are comparable with the literature examples [10, 19, 20].

The results of the axial compression test along with numerical results are presented first. Figure 6 shows the load-displacement curves in axial compression loading for configurations with 45° winding angle. The results for 1/1 and 2/1 mosaic patterns exhibit good repeatability both in the elastic part and when the damage started and propagated. In the case of configuration with 3/1 mosaic pattern, the load-displacement curve for one specimen was a bit deviated from the rest which may be caused by the initial slack of the specimen. This behaviour was observed in latter configurations also and it was concluded that it does not influence the final maximum force [21]. Irrespective of this, the tested tubes exhibit elastic behaviour in the first phase of the experiment. Then, a gradual degradation of the stiffness occurred caused by the damage of the material. The numerical results presented along with the experimental curves are in good agreement in terms of the maximum force achieved. However, it was observed that the numerical analysis was almost linear up to the final failure.

The configurations with 55° winding angle are presented in Figure 8. Satisfactory repeatability of the results is obtained in terms of the maximum force and the general specimen behaviour. Some of the samples exhibited a slight deviation at the initial stage of the experiment,

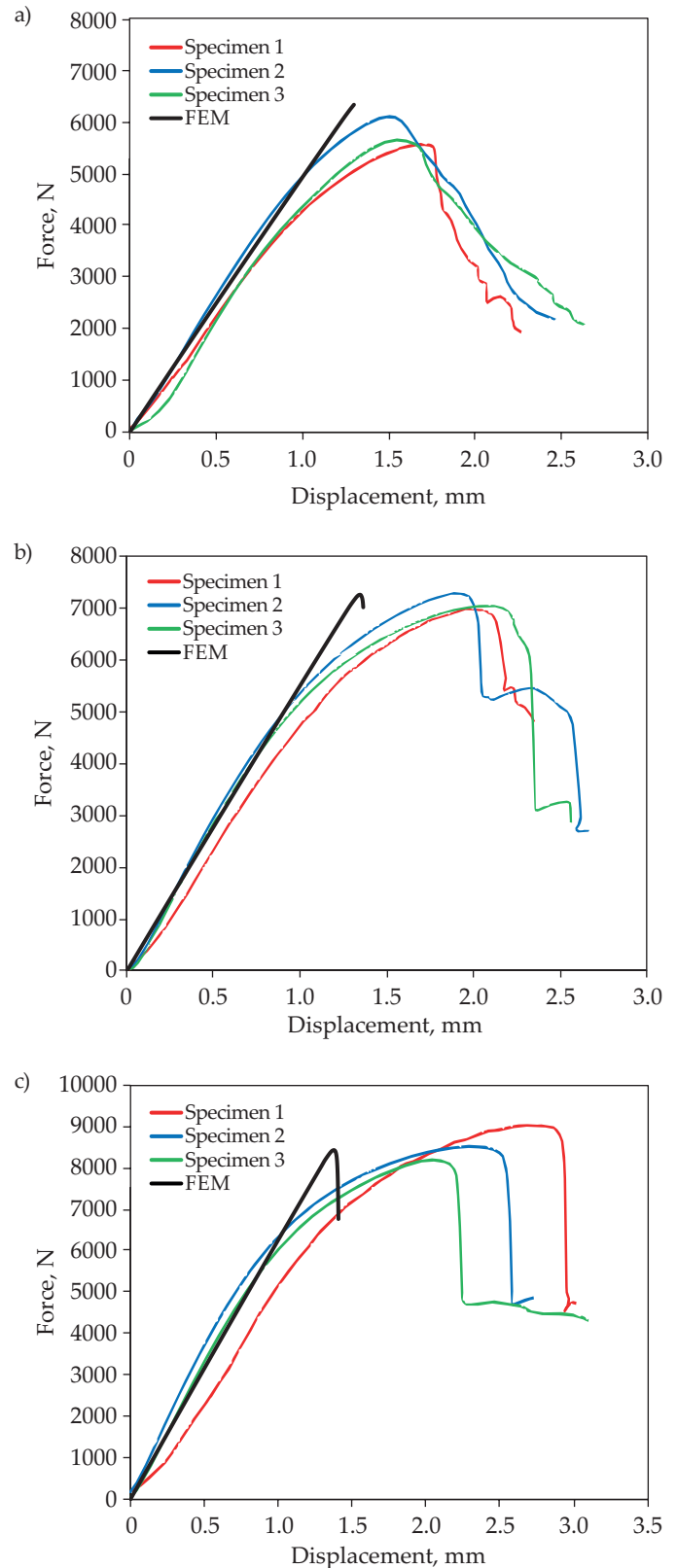


Fig. 6. Force-displacement curves for 45° winding angle: a) 45_1/1, b) 45_2/1, c) 45_3/1

as it was in the case of 45°, however, it did not influence the maximum force. The load-displacement curves present a more rapid failure without flattening, as could have been observed in the case of 45° specimens. The numerical analyses present slightly underestimated results in

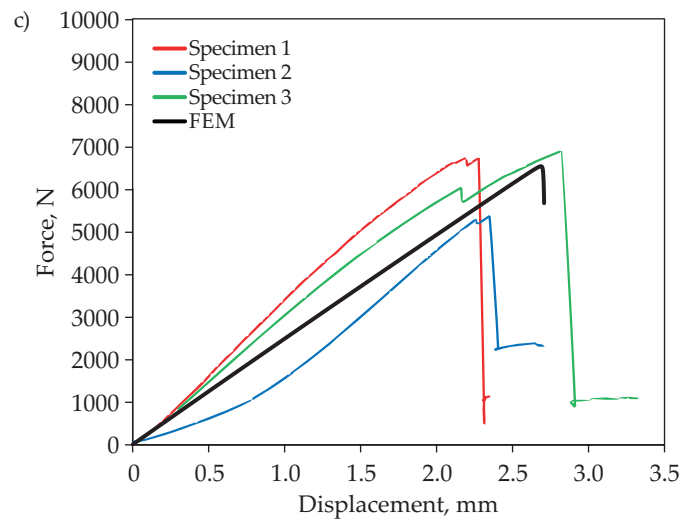
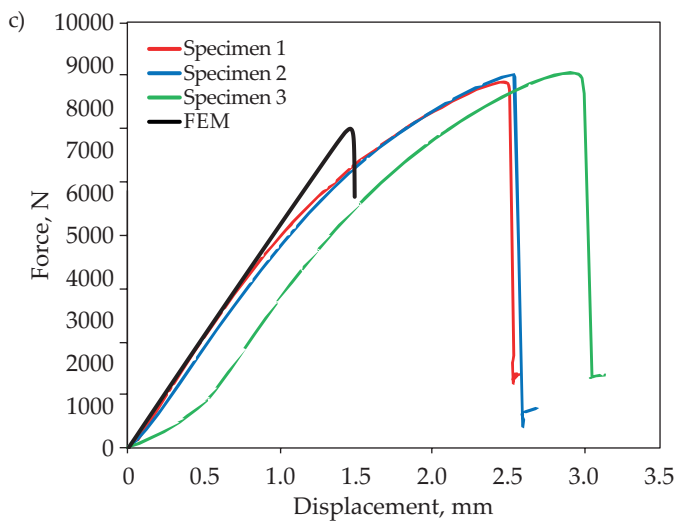
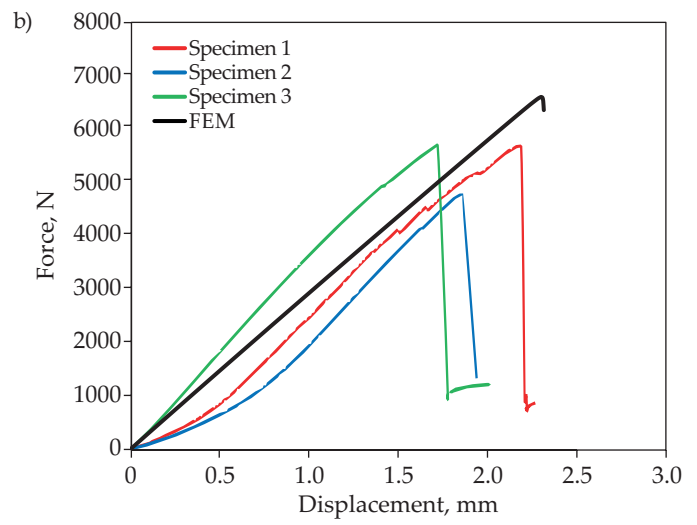
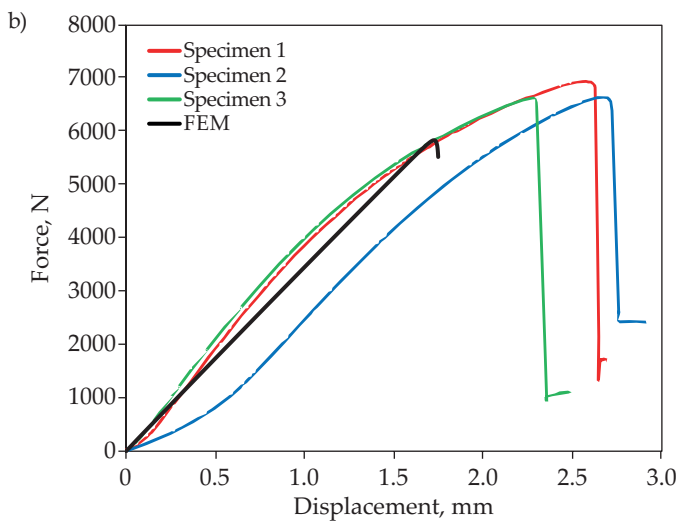
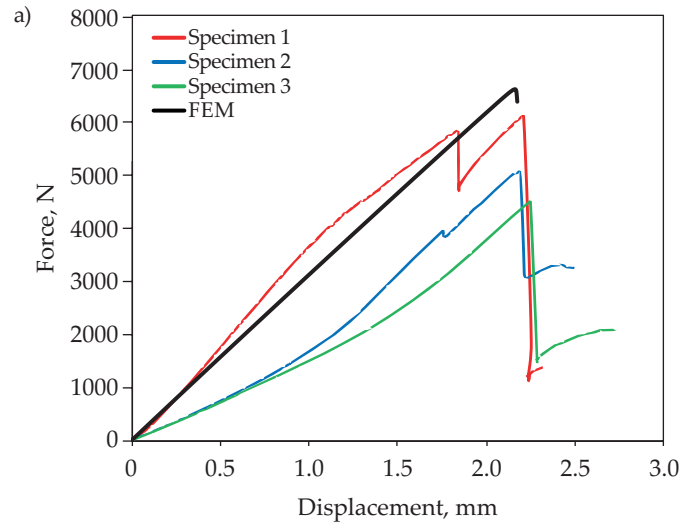
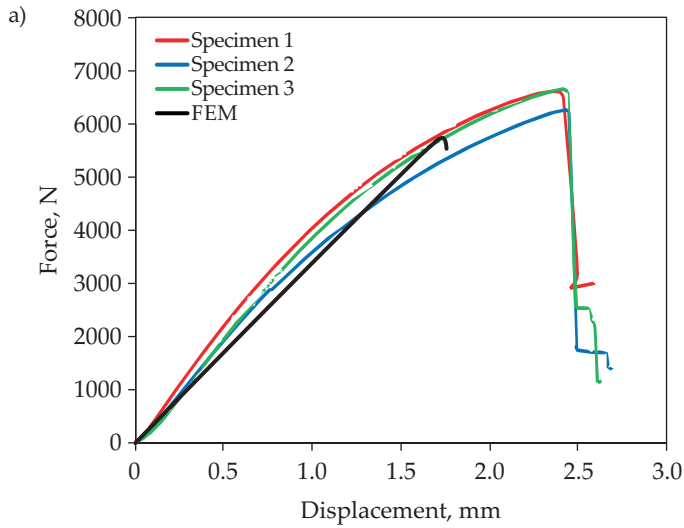


Fig. 7. Force-displacement curves for 55° winding angle:
a) 55_1/1, b) 55_2/1, c) 55_3/1

Fig. 8. Force-displacement curves for 75° winding angle:
a) 75_1/1, b) 75_2/1, c) 75_3/1

terms of maximum force, however, within an acceptable deviation.

Figure 8 shows the results of the axial compression test for a winding angle of 75°. In this case, higher deviation of maximum force was observed. In general, the

samples presented more unstable behaviour with some rapid drops of compressing force but without final failure. It may be seen for 1/1 configuration, where specimen 1 reaches the maximum force, then rapidly falls to about 1000 N and once again gains the maximum force

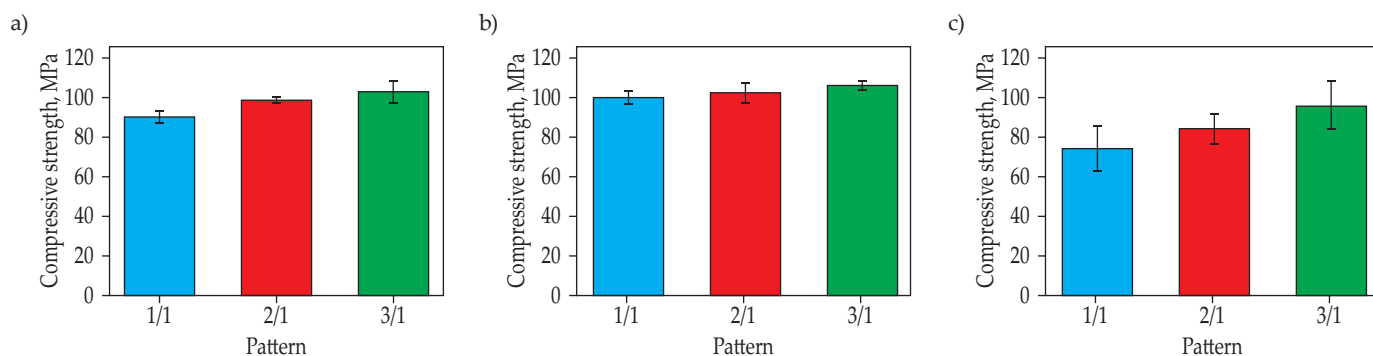


Fig. 9. Compressive strength for different patterns and winding angles: a) 45°, b) 55°, c) 75°

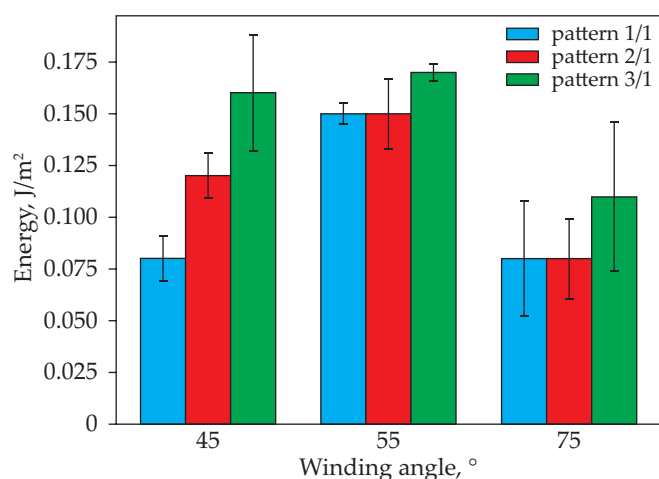


Fig. 10. Corrected absorbed energy for each configuration in the axial compression test

after which final failure occurs. Most samples exhibited almost linear behaviour up to the failure. Numerical analyses were slightly overestimating the maximum force in the case of 1/1 and 2/1 mosaic pattern configuration. In 3/1 configuration, FEM results reflected the experimental data accurately.

To quantitatively compare the results, it was decided to calculate the compressive strength of the specific configurations following Equation 1:

$$\sigma_c = \frac{F_{max}}{A} \quad (1)$$

where F_{max} is the maximum force obtained during the test and A is the area of the tube. The results are presented in Figure 9.

An additional parameter that was considered was the corrected absorbed energy. The energy was calculated as the area under the load-displacement curves divided by the cross-section of the specimen. The results are shown in Figure 10.

Table 5 summarizes the quantitative comparison of the filament-wound tubes subjected to axial compression loading. For each configuration, compressive strength and corrected absorbed energy are presented. The increase or decrease relative to the basic 1/1 mosaic pattern is calculated. In each winding angle, there is a positive correlation between the specific mechanical parameter and mosaic pattern [22]. The biggest growth was observed by a winding angle of 45° in the case of energy.

Table 5. Compressive strength and corrected absorbed energy values for examined samples

Configuration		σ_c , MPa	Dif., %	E, 1/m ²	Dif., %
45°	1/1	90.6 ± 3.2	ref.	0.08 ± 0.01	ref.
	2/1	98.8 ± 1.7	9.1	0.12 ± 0.01	47.0
	3/1	103.3 ± 5.6	14.0	0.16 ± 0.03	90.9
55°	1/1	102.3 ± 2.9	ref.	0.15 ± 0.01	ref.
	2/1	105 ± 5.1	2.6	0.15 ± 0.02	1.2
	3/1	108.7 ± 2.4	6.3	0.17 ± 0.01	11.3
75°	1/1	78.0 ± 12.0	ref.	0.08 ± 0.03	ref.
	2/1	88.3 ± 7.9	13.3	0.08 ± 0.02	-2.4
	3/1	100.7 ± 12.8	29.1	0.11 ± 0.04	30.7

Dif. – relative difference to the reference pattern 1/1 for each winding angle

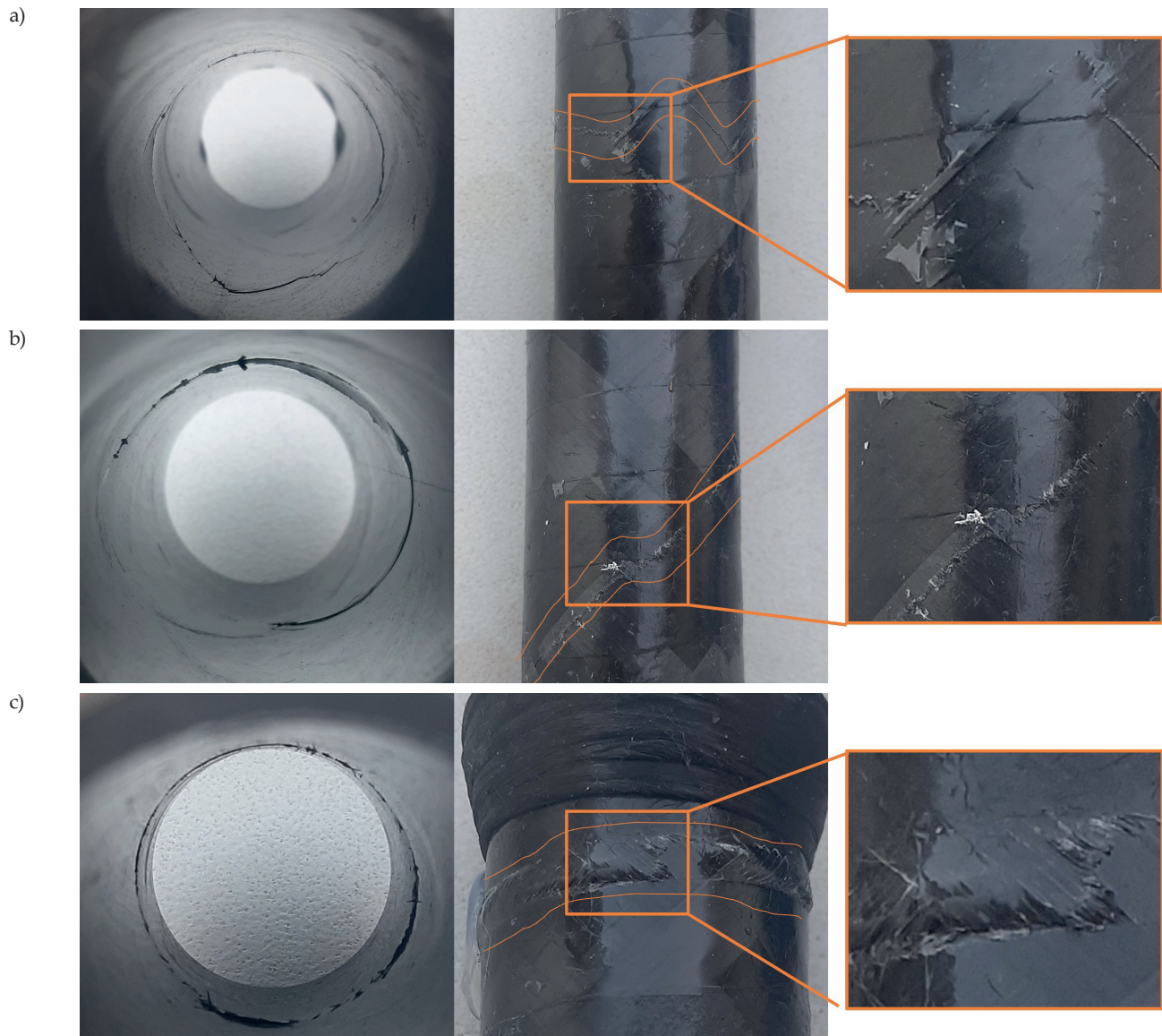


Fig. 11. Different types of fracture path on 45° winding angle samples: a) 45_1/1, b) 45_2/1, c) 45_3/1

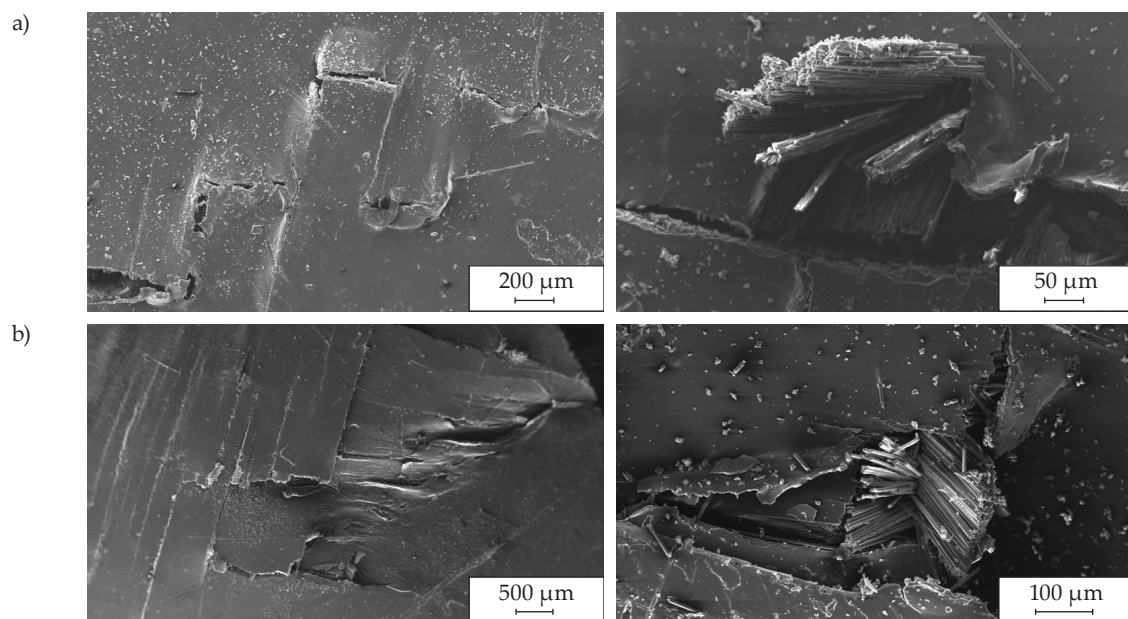


Fig. 12. SEM images of inner surface for axially compressed specimens: a) 45_1/1, 45_2/1

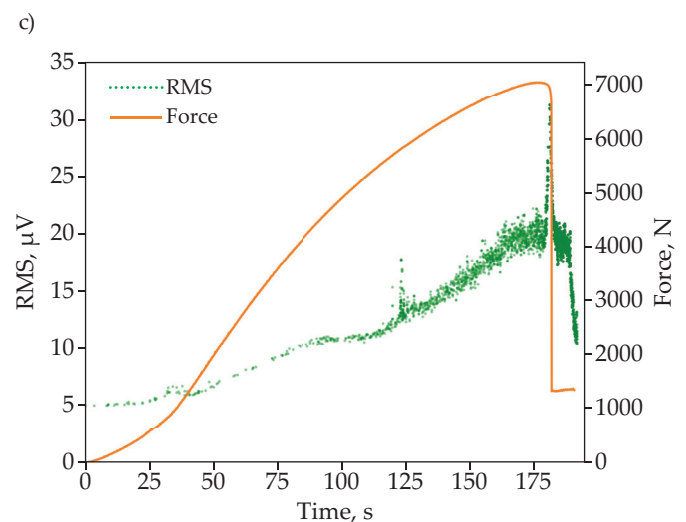
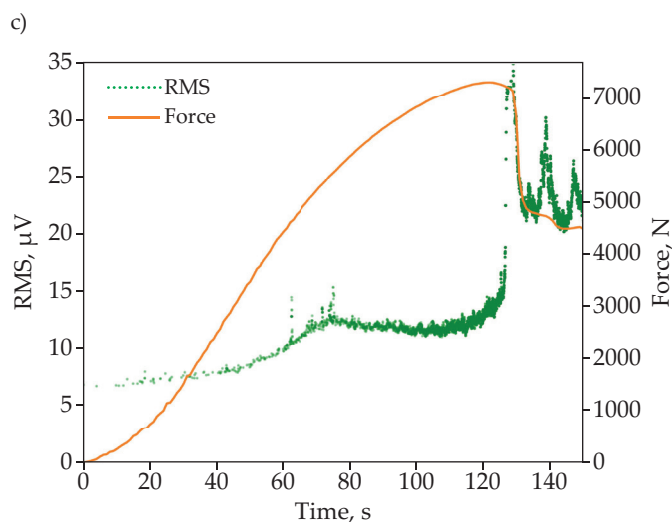
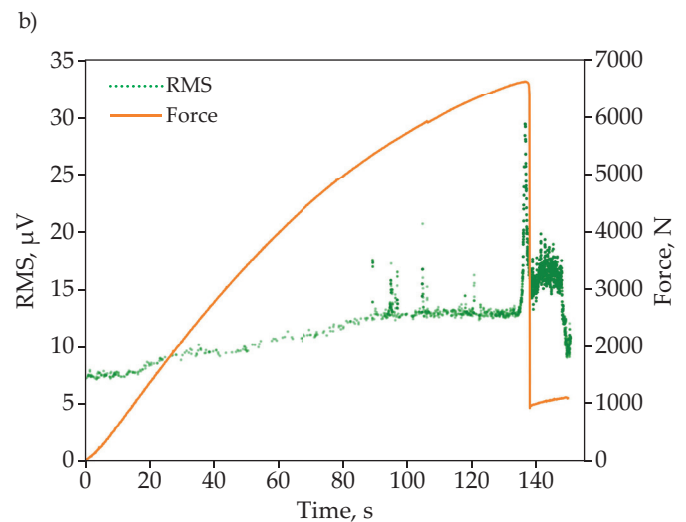
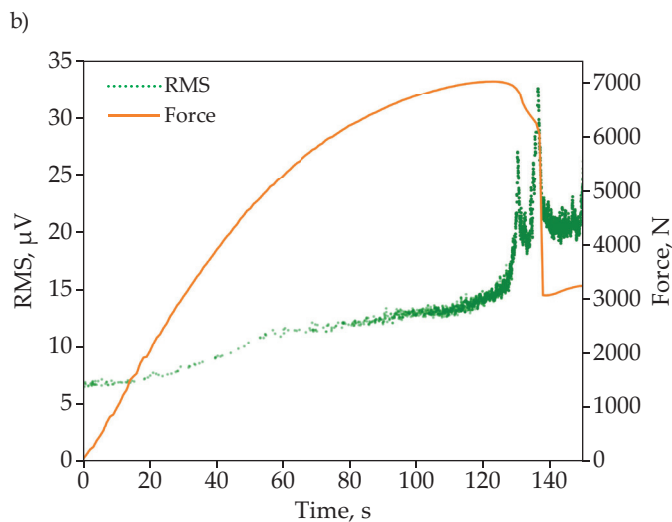
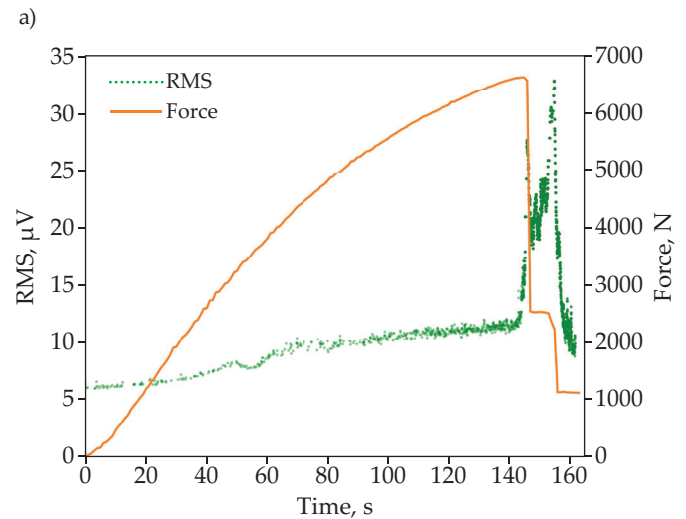
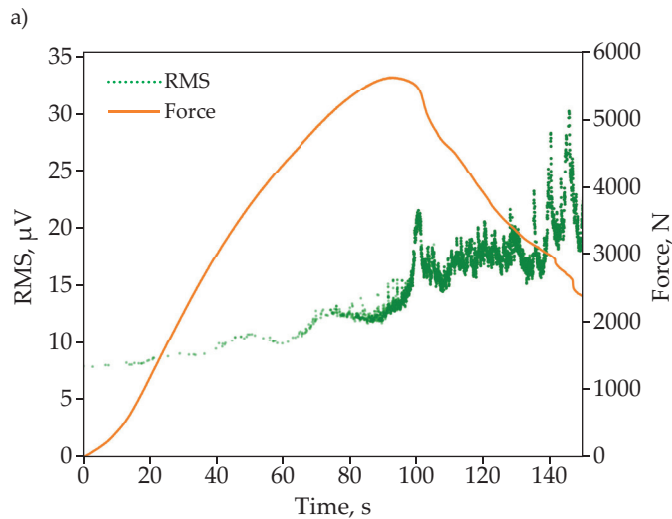


Fig. 13. Acoustic emission results for 45° winding angle samples: a) 45_1/1, b) 45_2/1, c) 45_3/1

Fig. 14. Acoustic emission results for 55° winding angle samples: a) 55_1/1, b) 55_2/1, c) 45_3/1

Microscopic observations and acoustic emission

Macroscopic observations of the tested specimens reveal different fracture paths. Exemplary results are shown in Figure 11 on the example of 45° winding

angle. In the case of a low mosaic pattern, where the laminate area is bigger, the fracture path looked more like a straight line following the fiber direction. In the same cases, the shape was more polygonal line-like, as may be seen in Figure 12 and 1/1 mosaic pattern. For

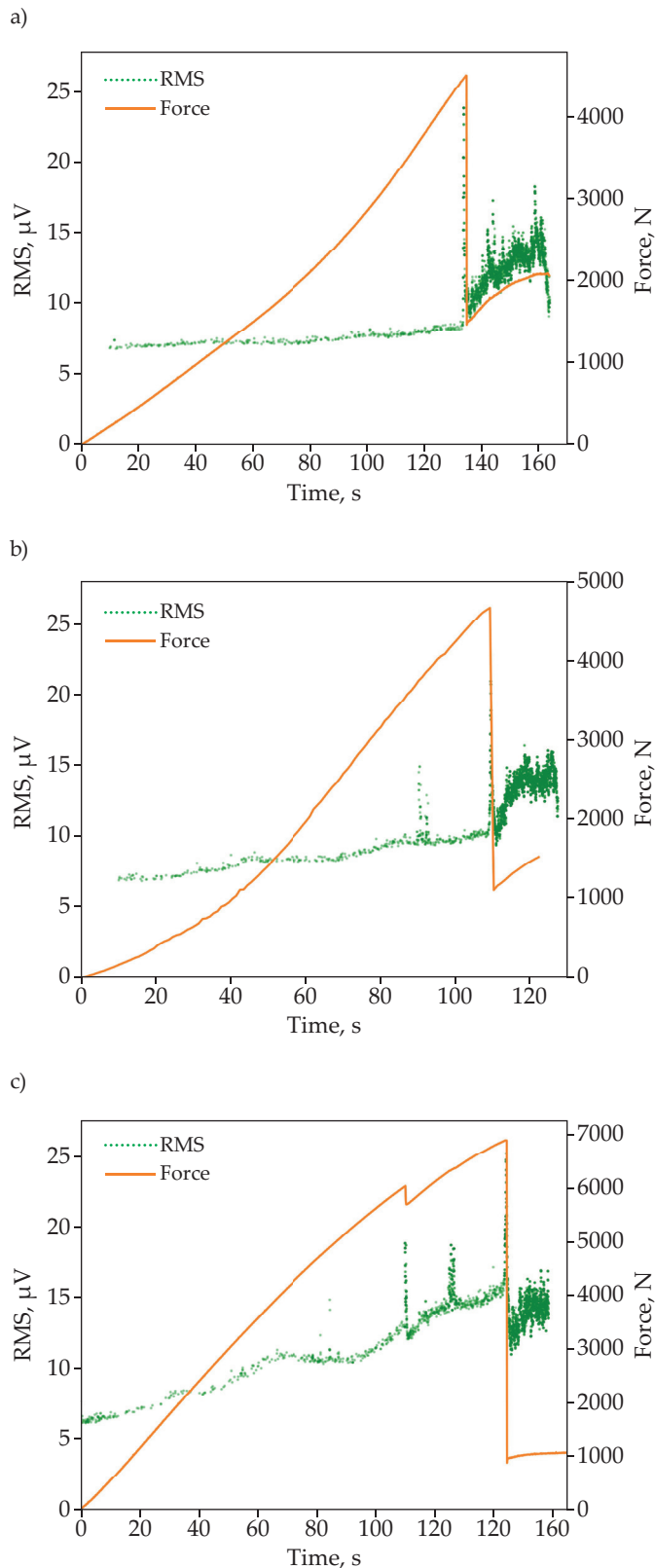


Fig. 15. Acoustic emission results for 75° winding angle samples: a) 75_1/1, b) 75_2/1, c) 75_3/1

a higher number of mosaic patterns like 3/1, the number of interlaces restricted the crack propagation along the fiber direction which caused a failure in the hoop direction, as it is shown in the figure below [22]. However, this is not a rule, since for some different specimens

of the configuration 45° 3/1 the path followed the fiber direction.

Microscopic observations were carried out on the inner layer of the specimens. SEM images presented in Fig. 12. present a typical for composite materials damage modes: delamination, micro-buckling, kinking and fiber breakage [23, 24].

Acoustic emission analysis was based on the root mean square (RMS) parameter. The RMS indicates the general activity of acoustic emission, also sometimes described as acoustic power [23, 25–29]. Fig. 13–15 shows the AE results of the axial compression test for specimens with three mosaic patterns and 45°, 55° and 75° winding angles.

The AE results for 45° winding angle exhibit no significant differences in terms of the RMS parameter. In each case, a very low intensity of the signal is presented in the initial phase of the experiment and rises slowly up to the moment, when the force-displacement curve starts to present regressive tendency. Therefore, it may be concluded that with the loss of specimen stiffness, the material starts to damage more severely. A rapid growth of the AE events is observed during the failure moment [30, 31].

For 55° winding angle, the dependency between the mosaic pattern and the AE signals in terms of the RMS parameter is more noticeable compared to specimens with 45° winding angle. Figure 14 shows the relative to 1/1 growth of RMS in the case of 2/1 and even more to 3/1 mosaic pattern.

For a configuration with 75° winding angle, the impact of the higher mosaic pattern is also more visible compared to specimens with 45° winding angle. In the case of 1/1 mosaic pattern, the RMS parameter maintains very low up to the final failure of the specimen. Very few signals were acquired before the material collapse, which indicates that the damage did not propagate but happened suddenly with a rupturing loss of stiffness. For 2/1 mosaic pattern, a slight increase in the RMS parameter was observed before the failure. Finally, the most significant growth of RMS was visible in the case of 3/1 configuration, exhibiting an almost linear rise of AE signals throughout the experiment.

CONCLUSIONS

Axial compression loading was subjected to filament-wound tubes both in experimental and numerical approaches. The experimental part was equipped with acoustic emission testing also. Nine configurations were evaluated and compared using the following indicators: compressive strength and corrected absorbed energy. The macroscopic and microscopic observations were conducted to determine the failure modes occurring in the material. The higher the mosaic pattern number, the higher the compressive strength of the specimen was obtained. A similar trend was noticed in the case of corrected absorbed energy. The numerical results were in good agreement with the experimental curves, although

some discrepancies occurred. It was found that the deviations were due to the limitations of the FEA model, which did not consider the delamination failure mode. Moreover, the deterministic model did not consider the imperfections included in the material, which were visible in the microscopic images of the cross-section areas. The acoustic emission analysis was conducted by observing the shape of the RMS plot versus the load curve. The higher the winding angle, the higher the influence of mosaic pattern on the AE events intensity. Namely, for specimens with winding angle of 45°, the differences between the mosaic patterns were not so clear as it was in the case of 75° winding angle.

Authors contribution

P.S. – conceptualization, methodology, validation, investigation, writing-original draft, writing-review and editing, visualization; M.S. – methodology, writing-original draft, visualization, writing-review and editing; S.D. – investigation, writing-original draft, methodology; P.Z. – investigation, validation; K.P. – conceptualization, writing-review and editing; Z.P. – conceptualization, writing-review and editing; M.B. – conceptualization, supervision; W.B. – conceptualization, supervision.

Funding

Presented research results were obtained as part of the research task titled: “Assessment of the Strength of Composite Pipes under Axial Compression Using Acoustic Emission” financed from the pro-quality subsidy for the development of the research potential of the Faculty of Mechanical Engineering of the Wrocław University of Science and Technology in 2024.

Conflict of interest

The authors declare no conflict of interest.

Copyright © 2024 The publisher. Published by Łukasiewicz Research Network – Industrial Chemistry Institute. This article is an open access article distributed under the terms and conditions of the Creative Commons Attribution (CC BY-NC-ND) license (<https://creativecommons.org/licenses/by-nc-nd/4.0/>).



REFERENCES

- [1] Azeem M., Ya H.H., Alam M.A. *et al.*: *Journal of Energy Storage* **2022**, 49, 103468.
<https://doi.org/10.1016/j.est.2021.103468>
- [2] Błażejowski W., Barcikowski M., Stosiak M. *et al.*: *Alexandria Engineering Journal* **2024**, 91, 442.
<https://doi.org/10.1016/j.aej.2024.01.078>
- [3] Wu Q.G., Chen X.D., Fan Z.C. *et al.*: *Procedia Engineering* **2015**, 130, 32.
<https://doi.org/10.1016/j.proeng.2015.12.171>
- [4] Zhang Q., Xu H., Jia X. *et al.*: *Composite Structures* **2020**, 236, 111915.
<https://doi.org/10.1016/j.compstruct.2020.111915>
- [5] Lin S., Yang L., Xu H. *et al.*: *Composite Structures* **2021**, 255, 113046.
<https://doi.org/10.1016/j.compstruct.2020.113046>
- [6] Zu L., Xu H., Wang H. *et al.*: *Composite Structures* **2019**, 207, 41.
<https://doi.org/10.1016/j.compstruct.2018.09.007>
- [7] Zu L., Xu H., Jia X. *et al.*: *Composite Structures* **2020**, 235, 111766.
<https://doi.org/10.1016/j.compstruct.2019.111766>
- [8] Almeida Jr. J.H.S., Ribeiro M.L., Tita V. *et al.*: *Composite Structures* **2017**, 178, 20.
<https://doi.org/10.1016/j.compstruct.2017.07.054>
- [9] Martins L.A.L., Bastian F.L., Netto T.A.: *Materials and Design* **2013**, 49, 471.
<https://doi.org/10.1016/j.matdes.2013.01.026>
- [10] de Azevedo C.B., Almeida Jr. J.H.S., Eggers F. *et al.*: “On the importance of the filament winding pattern of composite cylinders in axial compression: damage and buckling analyses”, *Materials from 7th International Symposium on Solid Mechanics, Sao Carlos, Brazil April 15-17, 2019*.
<https://doi.org/10.26678/abcm.mecsol2019.msl19-0177>
- [11] Lisboa T.V., Almeida J.H.S., Spickenheuer A. *et al.*: *Thin-Walled Structures* **2022**, 173, 108954.
<https://doi.org/10.1016/j.tws.2022.108954>
- [12] Akhtar M.K., Qureshi W.A., Jamshed R. *et al.*: *Journal of Reinforced Plastics and Composites* **2021**, 40(17-18), 621.
<https://doi.org/10.1177/0731684421994326>
- [13] Pourahmadi E., Taheri-Behrooz F.: *International Journal of Mechanical Sciences* **2020**, 178, 105617.
<https://doi.org/10.1016/j.ijmecsci.2020.105617>
- [14] Taheri-Behrooz F., Pourahmadi E.: *Structural Engineering and Mechanics* **2019**, 72(6), 713.
<https://doi.org/10.12989/sem.2019.72.6.713>
- [15] Ye J., Yan Y, Li Y. *et al.*: *Composite Structures* **2020**, 242, 112141.
<https://doi.org/10.1016/j.compstruct.2020.112141>
- [16] <https://toray-cfe.com/wp-content/uploads/2020/12/toray-torayca-fibers-typical-properties.pdf> (access date 2.06.2024)
- [17] https://www.samaro.fr/app/uploads/2023/10/4b334b3392e7c6f80d7d3aee5a7d459134c33442ee6b_Araldite_LY_1564_Aradur_3474_eur_e-1.pdf (access date 2.06.2024)
- [18] Almeida Jr. J.H.S., St-Pierre L., Wang Z. *et al.*: *Composites Part B: Engineering* **2021**, 225, 109224.
<https://doi.org/10.1016/j.compositesb.2021.109224>
- [19] Almeida Jr. J.H.S., Souza S.D.B., Botelho E.C. *et al.*: *Journal of Materials Science* **2016**, 51, 4697.
<https://doi.org/10.1007/s10853-016-9787-9>
- [20] Reddy S.S., Yuvraj C., Rao K.P.: *International Journal of Composite Materials* **2015**, 5(5), 102.
<https://doi.org/10.5923/J.CMATERIALS.20150505.03>

- [21] Gemi D.S., Şahin Ö.S., Gemi L.: *Composite Structures* **2022**, 280, 114929.
<https://doi.org/10.1016/j.compstruct.2021.114929>
- [22] Lisboa T.V., Almeida Jr. J.H.S., Dalibor I.H. *et al.*: *Polymer Composites* **2020**, 41(6), 2446.
<https://doi.org/10.1002/pc.25548>
- [23] Smolnicki M., Duda S., Stabla P. *et al.*: *Composite Structures* **2022**, 294, 115810.
<https://doi.org/10.1016/j.compstruct.2022.115810>
- [24] Duda S., Smolnicki M., Osiecki T. *et al.*: *International Journal of Fracture* **2022**, 234, 213.
<https://doi.org/10.1007/s10704-021-00566-3>
- [25] Hussein E.: "Acoustic Emission" in "Non-destructive testing", Chulalongkorn University, Bangkok 1996, p. 125.
- [26] Unnthorsson R., Runarsson T.P., Jonsson M.T.: *International Journal of Fatigue* **2008**, 30(1), 11.
<https://doi.org/10.1016/j.ijfatigue.2007.02.024>
- [27] Liao B.B., Wang D.L., Hamdi M. *et al.*: *International Journal of Hydrogen Energy* **2019**, 44(40), 22494.
<https://doi.org/10.1016/j.ijhydene.2019.02.217>
- [28] Saeedifar M., Zarouchas D.: *Composites Part B: Engineering* **2020**, 195, 108039.
<https://doi.org/10.1016/j.compositesb.2020.108039>
- [29] Błachut A., Wollmann T., Panek M. *et al.*: *Composite Structures* **2023**, 304(Part 1), 116337.
<https://doi.org/10.1016/j.compstruct.2022.116337>
- [31] Alimirzaei S., Najafabadi M.A., Nikbakht A. *et al.*: *International Journal of Damage Mechanics* **2022**, 31(8), 1230.
<https://doi.org/10.1177/10567895221095603>
- [32] Alimirzaei S., Najafabadi M.A., Khodaei A.: *Applied Composite Materials* **2022**, 29, 1911.
<https://doi.org/10.1007/s10443-022-10049-w>

Received 5 XI 2024.

Accepted 20 XI 2024.

